

# Buckling Analysis of Rectangular Functionally Graded Plates with an Elliptic Hole Under Thermal Loads

R. Rezaei, A.R. Shaterzadeh<sup>\*</sup>, S. Abolghasemi

*Faculty of Mechanical Engineering, University of Shahrood, Shahrood, Iran*

Received 21 October 2014; accepted 28 December 2014

## ABSTRACT

This paper presents thermal buckling analysis of rectangular functionally graded plates (FG plates) with an eccentrically located elliptic cutout. The plate governing equations derived by the first order shear deformation theory (FSDT) and finite element formulation is developed to analyze the plate behavior subjected to a uniform temperature rise across plate thickness. It is assumed that the non-homogenous material properties vary through the plate thickness according to a power function. The developed finite element (FE) code with an extended mesh pattern is written in MATLAB software. The effects of aspect ratio of the plate, ellipse radii ratio, position and orientation of the cutout, boundary conditions (BCs) and volume fraction exponent are investigated in details. The results of present code are compared with those available in the literature and some useful design-orientated conclusions are achieved.

© 2015 IAU, Arak Branch. All rights reserved.

**Keywords:** FG plates; Thermal buckling; Finite element analysis; Elliptic hole

## 1 INTRODUCTION

**F**UNCTIONALLY graded materials (FGMs) provide useful applications due to their unique mechanical properties. These materials are typically composed of ceramic and metal, or a combination of different metals. FGMs are assembled by functionally grading the materials to have a smooth spatial variation of material composition. The full-ceramic face of the material is put in the location with high temperature and the other face consisting of pure metal is placed in the situation where mechanical properties, such as toughness, must be high. In various industries, plates with cutouts are widely used for various practical necessities such as venting, inspection, and providing easy access to engineering systems. These kinds of plates are often exposed to compressive loads due to utilization in thermal environments that can result in thermal buckling. Thus, the thermal buckling behavior of these plates with cutouts must be analyzed in order to impressively design such structures. In plates under uniform compression, the pre-buckling stress field is uniform everywhere in the plate; therefore analytical buckling solutions are easily obtained. While for plates with a cutout, the buckling analysis becomes very difficult since the presence of cutout causes the stress field in the plate to be non-uniform. Hence, the analytical buckling solutions are inaccessible, and various numerical methods need to be developed for analyzing such plates. Many investigations have been carried out to analyze the buckling behavior of FG plates. Bodaghi and Saidi [1] presented an analytical approach for buckling analysis of thick rectangular FG plates. They derived the equilibrium and stability equations according to the higher-order shear deformation plate theory. By introducing an analytical method, they converted the coupled governing stability equations into two uncoupled partial differential equations. Using Levy-type

<sup>\*</sup> Corresponding author. Tel.: +98 361 9995161.

*E-mail address:* ar.shaterzadeh@gmail.com (A.R. Shaterzadeh).

solution, they solved these equations for the FG plates with two opposite edges simply supported under different types of loading conditions. Samsam Shariat and Eslami [2] studied the thermal buckling of rectangular FG plates with geometrical imperfections. Using the classical plate theory (CPT), they obtained the equilibrium, stability, and compatibility equations of an imperfect FG plate. They employed the resulting equations to gain the closed-form solutions for the critical buckling temperature change of an imperfect FG plate. Weibgraeber et al. [3] used the closed-form analysis for the buckling behavior of an orthotropic plate with elastic clamping and edge reinforcement under uniform compressive load. All governing equations were transformed in a dimensionless system using common characteristic quantities to gain good analytical access. The buckling behavior was analyzed and generic buckling diagrams were presented. Zhao et al. [4] presented the mechanical and thermal buckling analysis of ceramic-metal FG plate. They employed the first-order shear deformation plate theory, in conjunction with the element-free kp-Ritz method. It was assumed that the material property of each plate varies exponentially through the thickness. They used the stabilized conforming nodal integration method to evaluate the bending stiffness, and calculated the membrane and shear stiffness using the direct nodal integration approach to avoid shear locking. They investigated the buckling responses of solid plates without hole under mechanical and thermal loads, and also plates with a centrally located hole under mechanical load. Ghosh and Kanoria [5] investigated thermo-elastic displacements and stresses in an FG spherically isotropic hollow sphere due to prescribed temperature in the context of the linear theory of generalized thermo-elasticity with two relaxation time parameters (Green and Lindsay theory). Mahdavian [6] studied mechanical buckling of rectangular FG plates. He derived equilibrium and stability equations of an FG plate under uniform in-plane compression on the basis of CPT. For isotropic materials, he presented convergent buckling loads for non-uniformly compressed rectangular plates based on a rigorous superposition Fourier solution for the in-plane Airy stress field and Galerkin's approach for stability analysis. Finally, he presented the results for a sample of FGM. Samsam Shariat and Eslami [7] investigated buckling analysis of rectangular FG plates under different types of mechanical and thermal loads. They used the third order shear deformation plate theory to derive the equilibrium and stability equations and obtained the closed-form solution for critical buckling load for various loading cases. It was assumed that the non-homogeneous mechanical properties vary linearly through the thickness of the plate. Xiang and Kang [8] dealt with the bending analysis of FG plates by an  $n$ th-order shear deformation theory and mesh-less global collocation method based on the thin plate spline radial basis function. They derived the governing equations by the principle of virtual work. They calculated the displacement and stresses of a simply supported FG plate under sinusoidal load to verify the accuracy and efficiency of their presented theory. Mozafaria and Ayob [9] considered the mechanical buckling load on a simply supported plate made of FGM with linearly varying thickness. Based on higher-order theory assumptions, they obtained the equilibrium and stability equations and the relations for pre-buckling loads of the plate under mechanical load by using a variational formulation. They derived the closed form solution for the buckling load. Raki et al. [10] derived the equilibrium and stability equations of a rectangular plate made of FGM under thermal loads based on the higher order shear deformation plate theory. Avci et al. [11] presented thermal buckling analysis of symmetric and anti-symmetric cross-ply laminated hybrid composite plate with a circular hole located in the plate center and subjected to a uniform temperature rise for different BCs. They employed the FSDT in conjunction with variational energy method in the mathematical formulation and used the eight-node Lagrangian finite element technique to find the thermal buckling temperature of hybrid laminates.

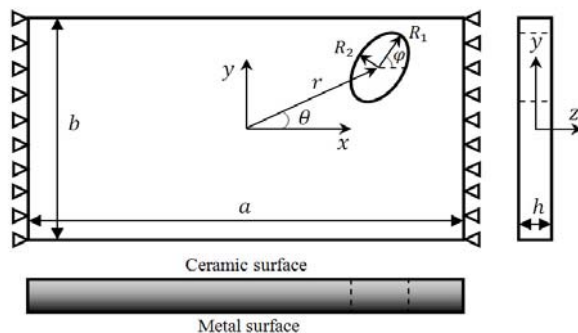
Zhen and Wanji [12] derived a single-layer higher-order model for predicting the stresses at curved free boundaries of laminated composite plates with a central circular hole subjected to in-plane loading. They considered a triangular finite element based on the proposed model and the methodology of the discrete Kirchhoff plate bending element. They showed that the proposed model is capable to predict in-plane and inter-laminar stresses around the circular hole. Kiani and Eslami [13] studied the buckling of heated annular FG plates on an elastic foundation analytically. They obtained the equilibrium equations of an annular-shaped plate based on the CPT. They proposed an exact analytical solution to calculate the thermal buckling load by obtaining the eigenvalues of the stability equation. Thai et. al [14] analyzed buckling of functionally graded plates based on a theory which accounts for a quadratic variation of the transverse shear strains across plate thickness and satisfies the zero traction BCs on the top and bottom surfaces of the plate without using shear correction factors. Thermal buckling of moderately thick FG plates with a central circular cutout has been investigated by Saji et.al [15]. The temperature distribution across plate thickness is represented by one dimensional head conduction equation and the critical buckling temperature for different values of power index, size of cutout and BCs is compared. In a recent work, buckling of functionally graded plates with internal cracks and cutouts has been investigated by Natarajan et. al [16]. They have performed a numerical study by using the extended finite element method and an enriched shear flexible 4-noded quadrilateral element for the spatial discretization. Zenkour and Mashat [17] studied thermal buckling response of functionally graded plates using sinusoidal shear deformation plate theory (SPT). They assumed the material properties of the

plate to vary according to a power law form in the thickness direction. They derived equilibrium and stability equations based on the SPT and solved the non-linear governing equations for plates subjected to simply supported BCs. They investigated the influences of plate parameters on buckling temperature difference. Saidi and Baferani [18] investigated thermal buckling analysis of moderately thick functionally graded annular sector plate. They derived the equilibrium and stability equations using first order shear deformation plate. By using an analytical method, they replaced the coupled stability equations by four decoupled equations. Solving the decoupled equations and satisfying the BCs, the critical buckling temperature was found analytically. They assumed that the annular sector plate is simply supported in radial edges and it has arbitrary BCs along the circular edges. They studied thermal buckling of functionally graded annular sector plate for two types of thermal loading, uniform temperature rise and gradient through the thickness.

Finally, they discussed the effects of plate and material parameters on the critical buckling temperature of functionally graded annular sector plates. To our best knowledge from the literature review, thermal buckling analysis of FG plates with elliptic hole, have not been carried out by the researchers. In this paper, thermal buckling analysis of rectangular FG plates with an eccentrically located elliptic cutout is investigated. The plate is subjected to a uniform temperature rise across the thickness. Using FSDT, a finite element formulation is derived for analysis of the perforated plate under thermal loading. After validating the results of present code for an FG plate without hole with the results obtained by other researchers, the influence of various parameters, such as aspect ratio and BCs of plate, size and position of cutout, and FGM properties are discussed in details and some useful conclusions are presented.

## 2 PROBLEM DEFINITION AND MESH LAYOUT

In Fig. 1 a rectangular FG plate with an eccentrically located elliptic hole is shown. The coordinates system is defined in a way that  $x, y$  and  $z$  axes are directed along length, width, and thickness of the plate, respectively. In this figure,  $a, b$  and  $h$  are the length, width, and thickness, respectively;  $R_1$  and  $R_2$  are the radii of the ellipse,  $r$  and  $\theta$  are the polar coordinates of the ellipse center; and  $\varphi$  which is the angle between the radius  $R_1$  and  $x$ -axis, represents the orientation of the elliptic cutout.



**Fig. 1**  
Geometry of an FG plate with an eccentrically located elliptical cutout.

Fig. 2 illustrates the mesh layout of the plate which is composed of two main distinct sections. The first section constitutes the whole plate that is composed of  $N_1$  and  $N_2$  elements along the length and width directions, respectively. The second section of the mesh is a rectangle which surrounds the cutout. This region contains the elements around the hole that is made up of  $2N_4$  elements along either  $x$  or  $y$  directions. Also a smaller sub-section with  $N_3$  elements is located in this section. In order to construct an appropriate mesh layout and investigate the convergence of the results, the values of all these parameters, i.e.  $N_1, N_2, N_3, N_4$  and the size of the surrounding mesh portion can readily be changed and consequently provides a flexible mesh pattern.

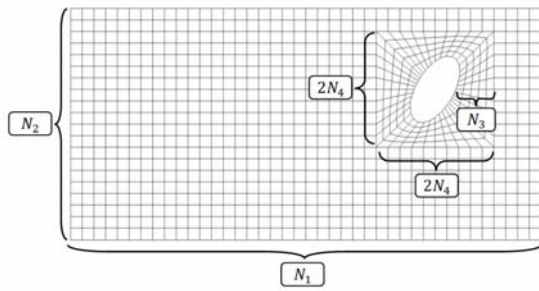


**Fig. 2**  
Mesh structure of the plate.

The number of total nodes  $N_n$  and total elements  $N_e$  in the mesh pattern are calculated as follows

$$\begin{aligned} N_n &= (N_1 + 1)(N_2 + 1) + 8N_3N_4 - (2N_4 - 1)^2 \\ N_e &= N_1N_2 + 8N_3N_4 - 4N_4^2 \end{aligned} \quad (1)$$

The different types of BCs which are used in this paper are expressed as:

Four edges clamped (CCCC):

$$\begin{aligned} u = w = \psi_y = \psi_x = 0 & \quad \text{for} \quad x = -a/2, a/2 \\ v = w = \psi_y = \psi_x = 0 & \quad \text{for} \quad y = -b/2, b/2 \end{aligned}$$

Two edges clamped (CC):

$$\begin{aligned} u = w = \psi_y = \psi_x = 0 & \quad \text{for} \quad x = -a/2, a/2 \\ w = 0 & \quad \text{for} \quad y = -b/2, b/2 \end{aligned}$$

### 3 THEORETICAL FORMULATION

The mechanical properties of FG plates change continuously along a certain direction which is usually taken to be thickness direction. By the power law, the volume fraction for a ceramic-metal FGM is expressed as [19]

$$\begin{aligned} V_c(z) &= \left( \frac{z}{h} + \frac{1}{2} \right)^n \quad 0 \leq n \leq \infty \\ V_c(z) + V_m(z) &= 1 \end{aligned} \quad (2)$$

In the above equation, the subscripts  $c$ ,  $m$  stand for ceramic and metal, respectively.  $V$  and  $n$  are the volume fraction of the constituent material and the volume fraction exponent for the ceramic, respectively. Also,  $h$  is the thickness of plate and  $z$  is the thickness coordinate ( $-h/2 \leq z \leq h/2$ ). Using the power law, material properties of FG plates can be written [20] as:

$$P(z) = (P_c - P_m)V_c(z) + P_m \quad (3)$$

where  $P$  is the effective material property which can be Young's modulus or coefficient of thermal expansion.

According to the FSDT, the displacement field is considered as the first order Taylor expansion of mid-plane variables with respect to plate thickness as follows [21]

$$u = u_0(x, y) + z\psi_x(x, y), \quad v = v_0(x, y) + z\psi_y(x, y), \quad w = w_0(x, y) \quad (4)$$

where  $u_0, v_0, w_0$  are displacements of a point located at mid-surface and  $\psi_x, \psi_y$  are rotations of a line initially normal to mid-plane, relative to  $y$  and  $x$  axes respectively. This displacement field causes a uniform shear strain in the thickness direction which is neglected in CPT and as a result, shear deformation theories are more accurate than CPT, especially for plates with bigger thickness to length ratio.

The strain tensor components for small strains but moderate rotations can be written [21] as:

$$\begin{aligned} \varepsilon_x &= \frac{\partial u}{\partial x} + \frac{1}{2} \left( \frac{\partial w}{\partial x} \right)^2, & \varepsilon_y &= \frac{\partial v}{\partial y} + \frac{1}{2} \left( \frac{\partial w}{\partial y} \right)^2, & \varepsilon_z &= \frac{\partial w}{\partial z} \\ \gamma_{xy} &= 2\varepsilon_{xy} = \left( \frac{\partial u}{\partial y} + \frac{\partial v}{\partial x} + \frac{\partial w}{\partial x} \frac{\partial w}{\partial y} \right), & \gamma_{xz} &= 2\varepsilon_{xz} = \left( \frac{\partial u}{\partial z} + \frac{\partial w}{\partial x} \right), & \gamma_{yz} &= 2\varepsilon_{yz} = \left( \frac{\partial v}{\partial z} + \frac{\partial w}{\partial y} \right) \end{aligned} \quad (5)$$

By substituting the displacement field from Eq. (4) in Eq. (5), the strain components are expressed as:

$$\begin{Bmatrix} \varepsilon_x \\ \varepsilon_y \\ \gamma_{xy} \end{Bmatrix} = \underbrace{\begin{Bmatrix} \frac{\partial u_0}{\partial x} \\ \frac{\partial v_0}{\partial y} \\ \frac{\partial u_0}{\partial y} + \frac{\partial v_0}{\partial x} \end{Bmatrix}}_{\varepsilon_1} + z \underbrace{\begin{Bmatrix} \frac{\partial \psi_x}{\partial x} \\ \frac{\partial \psi_y}{\partial y} \\ \frac{\partial \psi_x}{\partial y} + \frac{\partial \psi_y}{\partial x} \end{Bmatrix}}_{\varepsilon_2} + \underbrace{\begin{Bmatrix} \frac{1}{2} \left( \frac{\partial w}{\partial x} \right)^2 \\ \frac{1}{2} \left( \frac{\partial w}{\partial y} \right)^2 \\ \frac{\partial w}{\partial x} \frac{\partial w}{\partial y} \end{Bmatrix}}_{\varepsilon_{NL}}, \quad \begin{Bmatrix} \gamma_{xz} \\ \gamma_{yz} \end{Bmatrix} = \underbrace{\begin{Bmatrix} \frac{\partial w}{\partial x} + \psi_x \\ \frac{\partial w}{\partial y} + \psi_y \end{Bmatrix}}_{\varepsilon_3} \quad (6)$$

Here,  $\varepsilon_L$  and  $\varepsilon_{NL}$  are linear and nonlinear parts of strain components, respectively. Also the assumed displacement field causes the strain along thickness direction  $\varepsilon_z$  to be zero. According to hook's law for elastic materials and assuming plane-stress state, the stress-strain relations can be written as [14]

$$\begin{Bmatrix} \sigma_{xx} \\ \sigma_{yy} \\ \tau_{xy} \end{Bmatrix} = \begin{bmatrix} Q_{11} & Q_{12} & 0 \\ Q_{12} & Q_{22} & 0 \\ 0 & 0 & Q_{66} \end{bmatrix} \begin{Bmatrix} \varepsilon_{xx} - \alpha_x \Delta T \\ \varepsilon_{yy} - \alpha_y \Delta T \\ \gamma_{xy} - \alpha_{xy} \Delta T \end{Bmatrix}, \quad \begin{Bmatrix} \tau_{xz} \\ \tau_{yz} \end{Bmatrix} = \begin{bmatrix} Q_{44} & 0 \\ 0 & Q_{55} \end{bmatrix} \begin{Bmatrix} \gamma_{xz} \\ \gamma_{yz} \end{Bmatrix} \quad (7)$$

where  $\alpha_x, \alpha_y, \alpha_{xy}$  are the coefficients of thermal expansion and  $Q_{ij}$ 's are reduced stiffnesses for plane stress state which are function of mechanical properties of the material [14] as follows

$$Q_{11} = \frac{E(z)}{1-\nu^2}, \quad Q_{12} = \nu Q_{11}, \quad Q_{22} = Q_{11}, \quad Q_{44} = Q_{55} = Q_{66} = \frac{E(z)}{2(1+\nu)} \quad (8)$$

Here  $E$  is the Young's modulus that changes along plate thickness according to power law Eq. (3) and  $\nu$  is the Poisson's ratio which is assumed to be constant.

The in-plane stress vector  $\{\sigma_{xx} \ \sigma_{yy} \ \tau_{xy}\}^T$  includes mechanical  $\{\sigma_M\}$  and thermal  $\{\sigma_{Th}\}$  components as:

$$\{\sigma_M\} = [q]\{\varepsilon\}, \quad \{\sigma_{Th}\} = \mathbf{N}[q]\{\alpha\} \quad (9)$$

where

$$[q] = \begin{bmatrix} Q_{11} & Q_{12} & 0 \\ Q_{12} & Q_{22} & 0 \\ 0 & 0 & Q_{66} \end{bmatrix}, \quad \{\varepsilon\} = \begin{Bmatrix} \varepsilon_{xx} \\ \varepsilon_{yy} \\ \varepsilon_{xy} \end{Bmatrix}, \quad \{\alpha\} = \begin{Bmatrix} \alpha_x \\ \alpha_y \\ \alpha_{xy} \end{Bmatrix} \quad (10)$$

The total potential energy  $\Pi$  of plate is

$$\Pi = U + V \quad (11)$$

where  $U$  is strain energy related to linear part of strain tensor and  $V$  represents the work of in-plane forces during lateral deflection and is related to nonlinear part of strain tensor.

Strain energy ( $U$ ) can be calculated using the resultant force and moment vectors as:

$$U = \frac{1}{2} \iint \left( \{N\}^T \{\varepsilon_1\} + \{M\}^T \{\varepsilon_2\} + \{Q\}^T \{\varepsilon_3\} \right) dA - \iint \left( \{N_T\}^T \{\varepsilon_1\} + \{M_T\}^T \{\varepsilon_2\} \right) dA \quad (12)$$

In the above equation, resultant force and moment vectors are expressed as:

$$\{N, M\} = \int_{-h/2}^{h/2} \{\sigma_M\}(1, z) dz, \quad \{Q\} = k_s \int_{-h/2}^{h/2} \begin{Bmatrix} \tau_{xz} \\ \tau_{yz} \end{Bmatrix} dz, \quad \{N_T, M_T\} = \int_{-h/2}^{h/2} \{\sigma_{Th}\}(1, z) dz \quad (13)$$

where  $k_s$  (shear correction factor) is defined as  $k_s = \frac{5}{6 - \nu(V_c(z) + V_m(z))}$  [22]. After invoking the constitutive equations in Eq. (7), the resultant force and moment vectors can be written as:

$$\{N\} = [A]\{\varepsilon_1\} + [B]\{\varepsilon_2\}, \quad \{M\} = [B]\{\varepsilon_1\} + [D]\{\varepsilon_2\}, \quad \{Q\} = [A_s]\{\varepsilon_3\} \quad (14)$$

where

$$[A], [B], [D] = \int_{-h/2}^{h/2} [q](1, z, z^2) dz, \quad [A_s] = k_s \int_{-h/2}^{h/2} \begin{bmatrix} Q_{44} & 0 \\ 0 & Q_{55} \end{bmatrix} dz \quad (15)$$

By substituting Eq. (14) in Eq. (12) and simplifying the mathematical relations, the strain energy can be written as:

$$U = \frac{1}{2} \iint \left( \begin{Bmatrix} \varepsilon_1^T & \varepsilon_2^T \end{Bmatrix} \begin{bmatrix} A & B \\ B & D \end{bmatrix} \begin{Bmatrix} \varepsilon_1 \\ \varepsilon_2 \end{Bmatrix} + \{\varepsilon_3\}^T [A_s]^T \{\varepsilon_3\} \right) dA - \Delta T \iint \begin{Bmatrix} \varepsilon_1^T & \varepsilon_2^T \end{Bmatrix} [A \ B] \{\alpha\} dA \quad (16)$$

The work of in-plane forces ( $V$ ) is expressed as:

$$V = \frac{1}{2} \iint \left( N_x \left( \frac{\partial w}{\partial x} \right)^2 + N_y \left( \frac{\partial w}{\partial y} \right)^2 + 2N_{xy} \frac{\partial w}{\partial x} \frac{\partial w}{\partial y} \right) dA = \frac{1}{2} \iint \begin{bmatrix} \frac{\partial w}{\partial x} & \frac{\partial w}{\partial y} \end{bmatrix} \begin{bmatrix} N_x & N_{xy} \\ N_{xy} & N_y \end{bmatrix} \begin{bmatrix} \frac{\partial w}{\partial x} \\ \frac{\partial w}{\partial y} \end{bmatrix} dA \quad (17)$$

where  $\{N\} = \{N_x \ N_y \ N_{xy}\}^T$ .

### 3.1 Finite element formulation

As the first step in the solution of problem using FE method, the domain is meshed with quadrilateral elements since the presence of cutout inhibits a uniform mesh with rectangular elements. Quadrilateral elements are difficult to be integrated and in order to circumvent this difficulty, isoparametric element formulation [23] is used. Using appropriate shape functions, a square reference element in natural coordinate  $(s, t)$  is mapped into a quadrilateral element in global coordinate  $(x, y)$ . Here, each node has 5 degrees of freedom. In isoparametric formulation, the value of field variables  $(u_0, v_0, w, \psi_x, \psi_y)$  are interpolated in the domain of reference element using the same shape functions which are used for geometric mapping. So we have

$$\begin{bmatrix} x \\ y \\ u_0 \\ v_0 \\ w \\ \psi_x \\ \psi_y \end{bmatrix} = \sum_{i=1}^4 N_i \begin{bmatrix} x_i \\ y_i \\ u_{0i} \\ v_{0i} \\ w_i \\ \psi_{xi} \\ \psi_{yi} \end{bmatrix} \quad (18)$$

where  $x_i, y_i, u_{0i}, v_{0i}, w_i, \psi_{xi}, \psi_{yi}$  are the value of interpolated variables at element nodes. Also the shape functions are defined in natural coordinate of reference element as follows

$$N_1 = \frac{(1-s)(1-t)}{4}, \quad N_2 = \frac{(1+s)(1-t)}{4}, \quad N_3 = \frac{(1+s)(1+t)}{4}, \quad N_4 = \frac{(1-s)(1+t)}{4} \quad (19)$$

Using the Jacobean matrix of transformation, differentiation with respect to global coordinate can be related to differentiation with respect to natural coordinates as:

$$\begin{bmatrix} \frac{\partial(\quad)}{\partial x} \\ \frac{\partial(\quad)}{\partial y} \end{bmatrix} = J^{-1} \begin{bmatrix} \frac{\partial(\quad)}{\partial s} \\ \frac{\partial(\quad)}{\partial t} \end{bmatrix}, \quad J = \begin{bmatrix} \frac{\partial x}{\partial s} & \frac{\partial y}{\partial s} \\ \frac{\partial x}{\partial t} & \frac{\partial y}{\partial t} \end{bmatrix} \quad (20)$$

Now, strain components can be related to vector of nodal displacements

$$\begin{Bmatrix} \varepsilon_1 \\ \varepsilon_2 \end{Bmatrix} = [B_1] \{d\}, \quad \begin{Bmatrix} \varepsilon_3 \end{Bmatrix} = [B_3] \{d\}, \quad \begin{Bmatrix} \frac{\partial w}{\partial x} \\ \frac{\partial w}{\partial y} \end{Bmatrix} = [B_2] \{d\} \quad (21)$$

In which  $\{d\} = \{u_1 \ v_1 \ w_1 \ \psi_{x1} \ \psi_{y1} \ \dots \ \psi_{y4}\}^T$  is vector of nodal displacements and strain-displacement matrices  $[B_1], [B_2], [B_3]$  are a function of both natural coordinates  $(s, t)$  and global nodal coordinates of each element  $(x_i, y_i, i = 1, 2, 3, 4)$ . Now the total potential energy can be written in terms of nodal displacements

$$\begin{aligned}
U+V &= \frac{1}{2} \iint \left( \{d\}^T [B_1]^T \begin{bmatrix} A & B \\ B & D \end{bmatrix} [B_1] \{d\} + \{d\}^T [B_3]^T [A_s]^T [B_3] \{d\} \right) |J| dA \\
&+ \iint \left( \{d\}^T [B_2]^T \begin{bmatrix} N_x & N_{xy} \\ N_{xy} & N_y \end{bmatrix} [B_2] \{d\} \right) |J| dA - \Delta T \iint \{d\}^T [B_1]^T [A \ B] \{\alpha\} |J| dA
\end{aligned} \tag{22}$$

where  $dA = ds \cdot dt$  and integration is performed in the domain of reference element. According to the principle of minimum total potential energy, in equilibrium state, the derivative of total potential energy of the system with respect to the vector of nodal displacements, i.e.  $\frac{\partial(U+V)}{\partial\{d\}}$ , must be zero. By applying this principle to Eq. (22), we

have

$$\begin{aligned}
&\left( \iint \left( [B_1]^T \begin{bmatrix} A & B \\ B & D \end{bmatrix} [B_1] + [B_3]^T [A_s]^T [B_3] + [B_2]^T \begin{bmatrix} N_x & N_{xy} \\ N_{xy} & N_y \end{bmatrix} [B_2] \right) |J| dA \right) \{d\} \\
&= \Delta T \iint [B_1]^T [A \ B] \{\alpha\} |J| dA
\end{aligned} \tag{23}$$

which can be simplified to

$$\left( [K_b] + [K_s] + [K_g] \right) \{d\} = \{F\} \tag{24}$$

In the above equation, the bending, shear and geometric stiffness matrices and the thermal force vector are defined as:

$$\begin{aligned}
[K_b] &= \iint [B_1]^T \begin{bmatrix} A & B \\ B & D \end{bmatrix} [B_1] |J| dA \\
[K_s] &= \iint [B_3]^T [A_s]^T [B_3] |J| dA \\
[K_g] &= \iint [B_2]^T \begin{bmatrix} N_x & N_{xy} \\ N_{xy} & N_y \end{bmatrix} [B_2] |J| dA \\
\{F_T\} &= \Delta T \iint [B_1]^T [A \ B] \{\alpha\} |J| dA
\end{aligned} \tag{25}$$

The stiffness matrices and thermal force vector are calculated for each element and are assembled. Finally, the BCs are applied and reduced global stiffness matrices and force vector are obtained.

By eliminating the geometric stiffness matrix from Eq. (24), pre-buckling equation for deriving nodal displacement vector  $\{d\}$  is written as:

$$\left( [K_b] + [K_s] \right) \{d\} = \{F_T\} \tag{26}$$

Now the nodal displacements calculated from previous step, are used for calculating the geometric stiffness matrix, to achieve the global thermal buckling equation as:

$$\left( [K_b] + [K_s] + \Delta T_c [K'_g] \right) \{d\} = 0 \tag{27}$$

$[K'_g]$  is the geometric stiffness matrix for unit temperature rise. With solving the above eigenvalue problem, critical thermal buckling temperature ( $\Delta T_c$ ) and buckling mode shape  $\{d\}$  are obtained.

#### 4 RESULTS AND DISCUSSION

To illustrate the convergence of the finite element code, an FG plate with (CC) BCs containing a centrally located elliptic cutout is considered. The radii of the ellipse are  $R_1 = 12$  and  $R_2 = 6\text{ mm}$  and its direction is horizontal ( $\varphi = 0$ ). As shown in Fig. 3, the values of the mesh parameters are changed so that an acceptable convergent behavior is obtained. According to this figure, thermal buckling temperature doesn't change considerably by increasing the total number of elements beyond 204. Hence, the number of total elements is selected as  $N_e = 204$ .

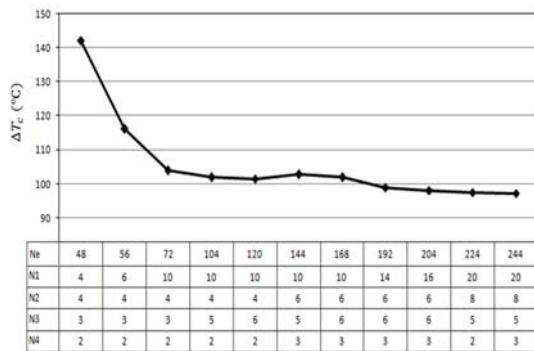


**Fig. 3** Convergence investigation of a rectangular plate of aspect ratio  $a/b=2.5$  with a centrally located elliptic cutout and (CC) BCs.

##### 4.1 Validation

In this section, to validate the developed FE code in this paper, two different cases are considered and the results are compared with those recorded by other researchers in literature. The material properties of the FG plates constituents are presented in Table 1.

**Table 1** Properties of the FGP constituents. [4]

Material	$E(\text{N/m}^2)$	$\nu$	Properties
			$\alpha(1/^\circ\text{C})$
Aluminum (Al)	$70.0 \times 10^9$	0.30	$23.0 \times 10^{-6}$
Alumina	$380.0 \times 10^9$	0.30	$7.4 \times 10^{-6}$

In first case, the critical thermal buckling temperature ( $\Delta T_c$ ) of a square aluminum/alumina FG plate ( $a/b = 1$ ) without hole for two different thickness ratios ( $a/h = 50$  and  $100$ ) is calculated for different values of volume fraction exponent ( $n$ ). The results are compared with Ref. [4] in Fig. 4. Both simply supported (SSSS) and fully clamped (CCCC) BCs are considered. As observed in Fig. 4, the  $\Delta T_c$  calculated from the present code are in good agreement with those reported in Ref. [4].

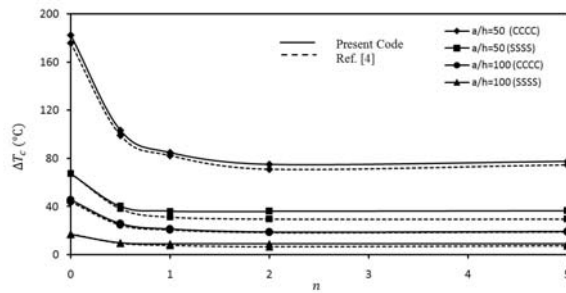


**Fig. 4**  
Comparison of critical thermal buckling temperature versus  $n$  for a square plate without hole with Ref. [4].

In second case, critical thermal buckling temperature of a rectangular aluminum/alumina FG plate without hole for two different aspect ratios  $a/b=0.25$  and  $0.5$  is compared with Ref. [7] and the results are presented in Fig.5. The BCs are simply supported and the material properties are presented in table 1. It can be seen that the proposed solution agrees well with the analytical solution that is developed by Ref. [7]. The discrepancy observed can be attributed to the difference in the solution method which is used by Ref. [7] and present work. This difference is reduced by reduction in plate thickness.

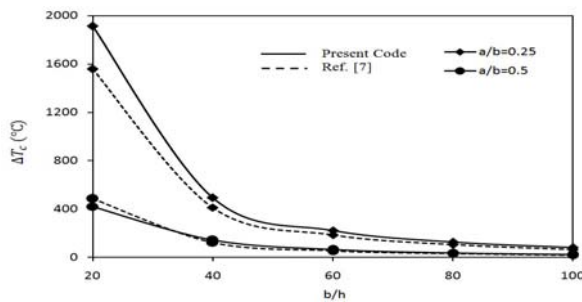


**Fig. 5**  
Comparison of critical thermal buckling temperature versus  $b/h$  for a rectangular plate without hole with Ref. [7].

## 4.2 Results

In this section, thermal buckling of FG plates with an elliptic cutout is investigated under uniform temperature rise across plate thickness by using the developed finite element code in preceding sections. The plates are composed of aluminum and alumina and their volume fraction changes across plate thickness. The properties of each constituent, including the Young's modulus, Poisson's ratio, and thermal expansion coefficient are presented in Table 1. The effects of different parameters on the critical thermal buckling temperature of FG plates are presented in following sections.

### 4.2.1 Influence of thickness ratio

To investigate the effect of thickness ratio ( $b/h$ ) on the critical buckling temperature, a square aluminum/alumina FG plate with an elliptic cutout in the center is considered. In order to effectively demonstrate this effect, plate-cutout area ratio ( $A_p/A_e$ ) is assumed constant and equal to  $A_p/A_e=20$ . However, the  $R_1/R_2$  ratio varies from 0 (without cutout case) to 3. Table 2. illustrates the variation of the critical buckling temperature of a square FG plate with/without elliptic cutout versus ellipse radii ratio  $R_1/R_2$ , for different plate thickness ratio under two (CC) and (CCCC) BCs. It is shown that the critical thermal buckling temperature decreases by the increase of thickness ratio because with decreasing thickness, strength of plate against buckling decreases. For the case of fully clamped plates whereas edges of plate are more constrained,  $\Delta T_c$  is lower than the CC clamped plates.

This shows that the FG plate with (CC) BCs is more resistant to thermal loads than CCCC one. For a specified value of plate thickness ( $b/h$ ), in the case of two edges clamped the critical buckling temperature is highest when

the radii ratio is 0.5. While for the case of four edges clamped the highest  $\Delta T_c$  occurs when  $R_1/R_2 = 3$ . In the case of fully clamped plates, for increasing the capacity of temperature endurance, one can extensive elliptic hole along the horizontal axes. For two edges clamped plates, this result is vice versa.

**Table 2**

Critical thermal buckling temperature ( $^{\circ}\text{C}$ ) of a square plate for various thickness ratio ( $b/h$ ), ellipse radii ratio ( $R_1/R_2$ ) and two BCs

(a) Two edges clamped					
$R_1/R_2$	$b/h = 20$	$b/h = 40$	$b/h = 60$	$b/h = 80$	$b/h = 100$
0	941.45	240.87	107.61	60.65	38.85
0.5	1053.12	270.24	120.81	68.11	43.63
1	927.70	237.15	105.89	59.67	38.22
1.5	891.20	227.84	101.73	57.32	36.72
2	871.79	222.97	99.58	56.12	35.95
2.5	858.65	219.80	98.19	55.34	35.45
3	849.34	217.58	97.22	54.80	35.11
(b) Four edges clamped					
$R_1/R_2$	$b/h = 20$	$b/h = 40$	$b/h = 60$	$b/h = 80$	$b/h = 100$
0	521.29	133.30	59.50	33.52	21.47
0.5	591.35	150.88	67.33	37.93	24.29
1	563.24	143.45	63.98	36.03	23.08
1.5	572.47	145.89	65.08	36.66	23.47
2	591.35	150.88	67.33	37.93	24.29
2.5	614.04	156.88	70.03	39.46	25.27
3	638.10	163.21	72.88	41.07	26.31

#### 4.2.2 Influence of aspect ratio and ellipse radii ratio

In this section, thermal buckling of an aluminum/alumina FG plate with a centrally located cutout is investigated for various aspect ratios and cutout sizes. Here, two different BCs and two different plate-cutout area ratios are considered and the effect of changing the values of  $a/b$  and  $R_1/R_2$  are examined for each case. It should be mentioned at this point that by increasing the plate-cutout area ratio the cutout size physically decreases relative to the plate area, and vice versa. In Fig. 6,  $\Delta T_c$  is depicted as a function of radii ratio for different aspect ratios of the plate. It can be seen that for both BCs and both plate-cutout area ratios,  $\Delta T_c$  increases with the growth of aspect ratio. For a specific value of  $R_1/R_2$  a square plate possesses the smallest critical buckling temperature and a rectangular plate with aspect ratio  $a/b=3$  has the largest one. For a constant area, circumference of a square is always smaller than a rectangular plate. Hence, in square plates the length of constrained boundary is smaller. Consequently, the plate resistance against transverse displacement and buckling due to thermal variation reduces and as a result thermal buckling temperature decreases.

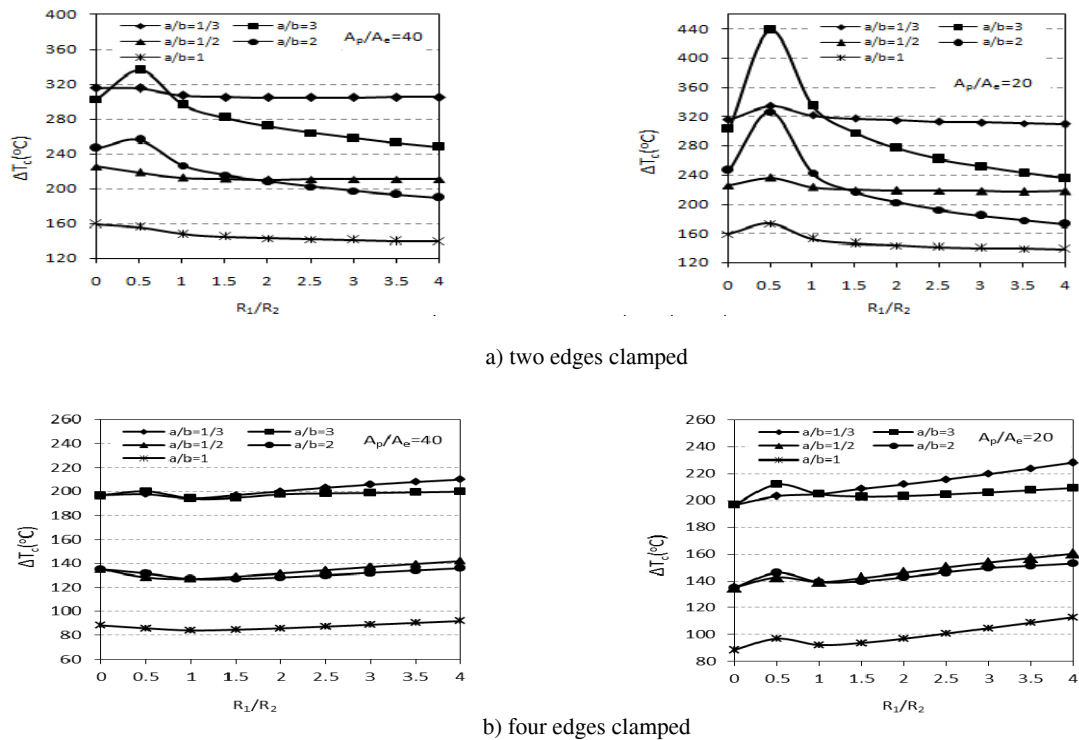


**Fig. 6**

Critical thermal buckling temperature of a rectangular plate for two different cutout sizes with various BCs.

with the aid of Fig. 6, since BCs in fully clamped plates are symmetric, one can see that the variation of critical buckling temperature versus radii ratio for CCCC plates is less intensive than that of CC plates. As another result, the critical buckling temperature for the case of  $R_1/R_2 = 0.5$  is higher than the case of plate without cutout, especially when the cutout area is bigger (i.e.  $A_p/A_e = 20$ ). For a plate with (CC) BCs, the highest critical buckling temperature is achieved for elliptical cutout with  $R_1/R_2 = 0.5$ . By increasing the  $R_1/R_2$  ratio beyond 0.5, the value of critical buckling temperature decreases. The interesting result is that a plate without a cutout has not always the highest critical buckling temperature. In fact, for some cases the plate with a cutout has higher resistance against thermal loading in comparison with a plate without a cutout which depends on BCs, area ratio, and cutout dimensions.

According to Fig. 6, the results of both aspect ratios 0.5 and 2 are similar for the symmetric (CCCC) BCs. The small difference between two graphs is due to the direction in which the cutout is stretched. In all of the cases, square plate has the lowest  $\Delta T_c$ . It can be seen that with decreasing  $A_p/A_e$  from 40 to 20, in other words by the growth of cutout size, the critical buckling temperature increases. Since BCs of hole are free, with increasing of hole size the plate can be deformed more easily due to increase in temperature, as a result thermal buckling temperature increases. For a specific cutout size, the critical buckling temperature is larger if the ellipse is stretched along the smaller edges of the plate. These interesting results can be considered at designing and constructing perforated plates in practical applications.

#### 4.2.3 Influence of cutout position and orientation

To investigate the influence of the cutout position and orientation ( $r, \theta$  and  $\varphi$  as shown in Fig. 1) on the thermal buckling behavior of the plate, the cutout is moved along three different directions: a) plate length direction  $\theta = 0^\circ$ ; b) plate diameter direction  $\theta = 45^\circ$ ; and c) plate width direction  $\theta = 90^\circ$ . For each direction, the cutout is relocated

in a different position by a certain increment. Moreover in each position the cutout is turned along center axes of the hole by three different angles  $\varphi = 0, 45$  and  $90$  degrees. Fig. 7 shows the plate with elliptic hole in an arbitrary position and orientation. In this figure, the parameter  $\eta$  is relative distance of the ellipse center from the plate center which is defined as  $\eta = r / s$ . The quantity  $s$  is defined as the distance from the plate center to the plate edge along the  $\theta$  direction.

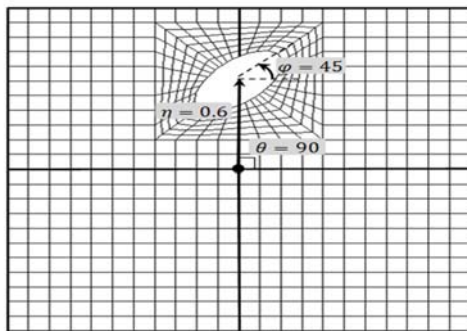


**Fig. 7**  
Plate with cutout in an arbitrary position and orientation.

In this section, a square aluminum/alumina plate with (CC) BCs containing an elliptic cutout with area ratio  $A_p / A_e = 40$  is considered. The ellipse radii ratio is assumed as  $R_1 / R_2 = 2$ . Fig. 8 depicts the variation of  $\Delta T_c$  versus the relative distance of the cutout center from the plate center  $\eta$ , for different positions and orientations of the cutout. As observed in Fig. 8 (a), the critical buckling temperature increases considerably by moving the cutout away from the plate center until nearly half the path.

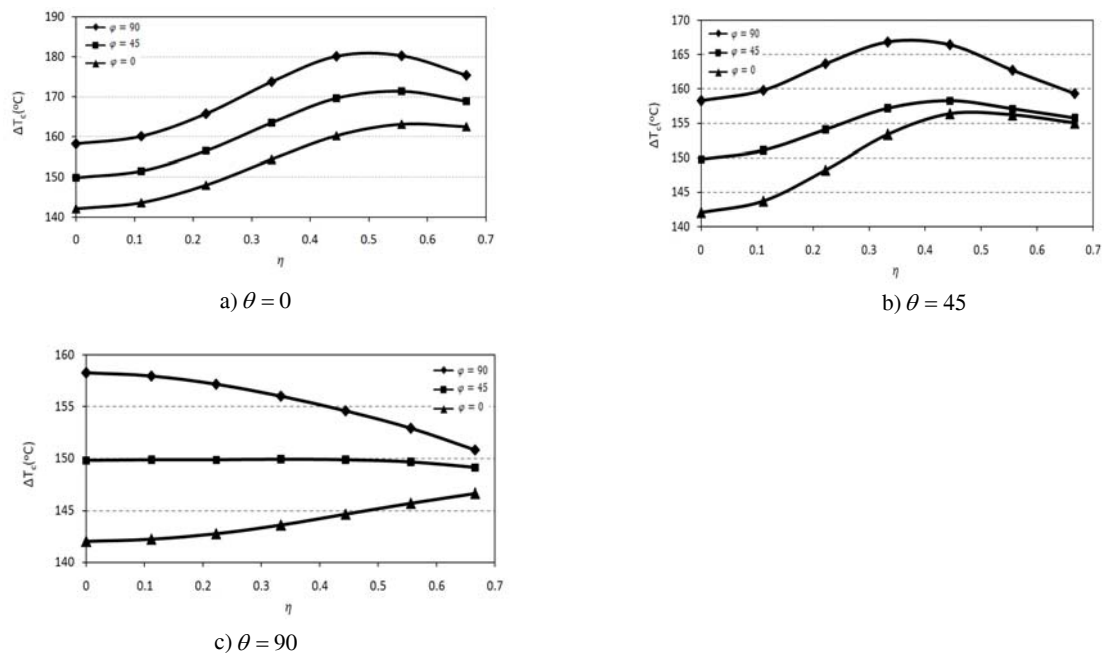


**Fig. 8**  
Influence of cutout position and orientation on critical buckling temperature of a square FG plate with an elliptic cutout under (CC) BCs for three different directions.

With more increasing  $\eta$ ,  $\Delta T_c$  insensibly decreases. Furthermore, the plate is more resistant to thermal loading when the cutout direction ( $\varphi$ ) is equal to  $90^\circ$ . Similar comments can be concluded for next case as seen in Fig. 8 (b) in which the cutout distance is increased along the plate diameter ( $\theta = 45^\circ$ ). As shown in Fig. 8 (c), when the cutout moves along the  $\theta = 90^\circ$  direction, namely the cutout is moving toward the non-clamped edges which are less resistant against deformation, the plate behavior is dissimilar. For  $\varphi = 45^\circ$ ,  $\Delta T_c$  does not change considerably relative to  $\eta$ . It can be seen that the highest critical buckling temperature is occurred when  $\varphi = 90^\circ$  and  $\eta = 0$ .

In each case,  $\varphi = 90^\circ$  has the highest  $\Delta T_c$ . Because of clamped BCs constraint more than simply supported BCs and with notice to free BCs on hole edges, if bigger diameter of hole is parallel to clamped edges ( $\varphi = 90^\circ$ ) the plate can be deformed more easily due to rising temperature, hence thermal buckling temperature rises.

It is seen that in the case ( $\varphi = 90^\circ, \theta = 0$ ),  $\Delta T_c$  is larger than two other directions ( $\theta = 45^\circ, 90^\circ$ ). Hence, this direction is the most appropriate one to locate the cutout along it; and  $\eta = 0.5$  is the best position for placing cutout center. In other words, the perforated plates have the highest resistance against thermal loading if the cutout is located in the position  $\theta = 0, \eta = 0.5$  and orientated at  $\varphi = 90^\circ$ .

#### 4.2.4 Influence of volume fraction exponent

In this section, the influence of the volume fraction exponent  $n$  on the critical buckling temperature is investigated. According to Eq. (2), when the value of  $n$  approaches to zero, the portion of ceramic in the plate material increases. When the value of  $n$  is equal to zero, the FG plate converts to an isotropic ceramic plate. On the other hand, by increasing  $n$ , the metal content of the FG plate increases. For the infinity value of  $n$  the FG plate becomes an isotropic metal plate. A square FG plate with a centrally located elliptic cutout is considered for two different BCs, i.e. (CC) and (CCCC). The thickness ratio, ellipse radii ratio, and aspect ratio are assumed as  $b/h = 50$ ,  $R_1/R_2 = 2$  and  $a/b = 1$ , respectively. The numerical results for  $\Delta T_c$  is depicted in Fig. 9.

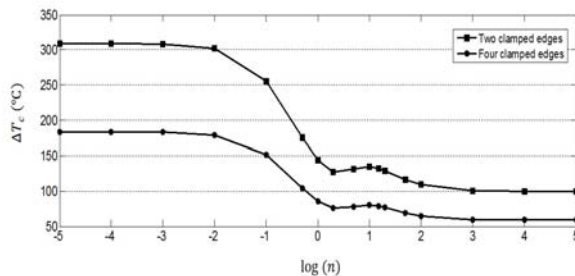


**Fig. 9**

Critical buckling temperature of a square FG plate with a centrally located elliptic cutout for various BCs versus  $n$ .

As observed in this figure, the critical buckling temperature decreases by increasing the volume fraction exponent and it converges to a constant value. This constant value is equal to the critical buckling temperature of the isotropic plate made of aluminum which is a special case of FG plate. The constant values are equal to  $\Delta T_c = 99.38^\circ\text{C}$  and  $58.99^\circ\text{C}$  for CC and CCCC conditions, respectively. On the other hand, by decreasing the value of  $n$  towards zero, the critical buckling temperature increases and converges to the special case one, namely the ceramic isotropic plate. This value is equal to  $\Delta T_c = 308.89^\circ\text{C}$  for CC condition and  $183.35^\circ\text{C}$  for CCCC condition.

#### 4.2.5 Mode shapes

First buckling mode shapes of FG plates for different cutout locations with (CC) and (CCCC) BCs are depicted in Figs. 10 and 11 respectively. It can be seen that for the CC case, the half sine waves are formed along the edges

which are clamped. The reason of this phenomenon can be explained as follows. The fully clamped edges 1 and 2 as shown in Fig. 10 (b) stand against plate deformation. Consequently, the plate deforms towards two other edges which are not completely fixed. While in the CCCC case, the half sine waves are occurred along the plate diameters since the BCS of the plate is symmetric.

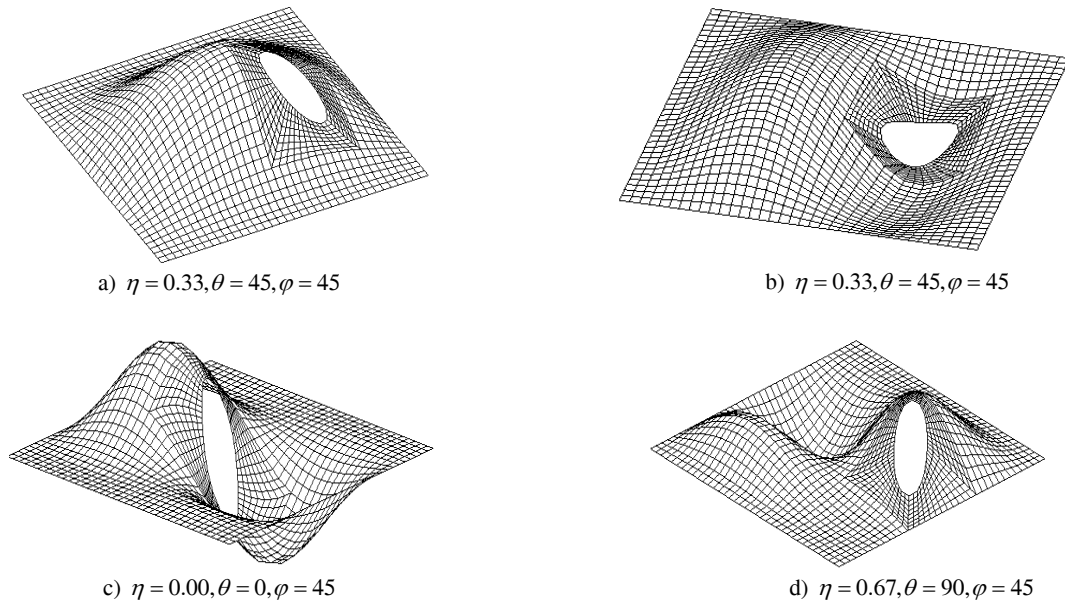


**Fig. 10** First four buckling mode shapes of FG plates with an elliptic cutout with (CC) BCs for various cutout locations.

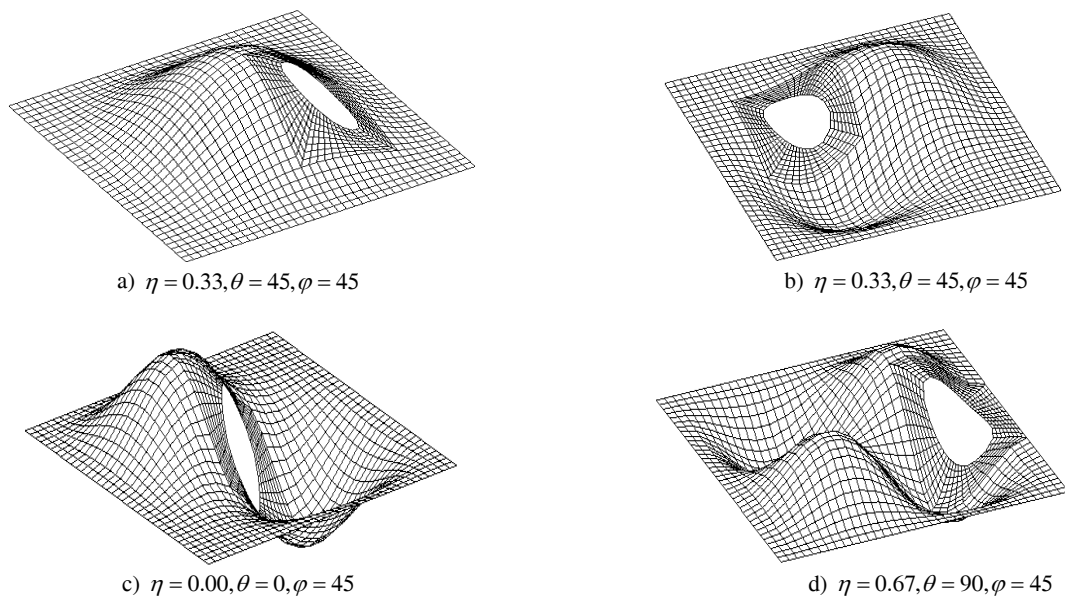


**Fig. 11** First four buckling mode shapes of FG plates with an elliptic cutout with (CCCC) BCs for various cutout locations.

## 5 CONCLUSIONS

In the present paper, buckling analysis of FG plates with a centrally/eccentrically located elliptic cutout under thermal loads was investigated. Mathematical derivations are based on first order shear deformation theory and nonlinear composition of the constituent materials. A finite element formulation was developed to analyze the material thermal behavior subjected to a uniform temperature rise by using an appropriate designed mesh structure. The influences of plate aspect ratio, plate-cutout area ratio, ellipse radii ratio, the position and orientation of hole, boundary conditions, and volume fraction exponent were inspected. The followings remarks are concluded:

- The critical thermal buckling temperature grows by increasing the plate thickness.
- The critical buckling temperature of an FG plate without/with cutout increases by increasing the value of plate aspect ratio from 1 to 3. In other words, thermal buckling strength of a rectangular plate is superior to a square plate with the same area. Briefly, whatever the aspect ratio ( $a/b$  or  $b/a$ ) is larger than one, the rectangular plate would be more resistant against thermal buckling.
- A plate without a cutout doesn't always have the highest critical buckling temperature. In fact, presence of a cutout in a rectangular plate can result in increasing thermal buckling strength of the plate. It depends on boundary conditions, aspect ratio, cutout size, and ellipse radii ratio.
- By increasing the size of the cutout, the critical buckling temperature increases.
- For a specific cutout size, the critical thermal buckling temperature increases by stretching the elliptic hole along the smaller edge of the plate.
- For two clamped edges plates, the critical thermal buckling temperature is much higher than that of fully clamped case.
- The position and orientation of the cutout have a considerable effect on the thermal strength of the plate. Based on the obtained results in present work  $\theta=0, \eta=0.5$  and  $\varphi=45^\circ$  is the best location for placing cutout for two clamped edges. In this position, the cutout is close to the clamped edges and is stretched toward the non-clamped edges.
- The half sine waves are formed along two clamped edges for CC boundary conditions, while it occurred along the plate diameters for fully clamped case.
- The critical buckling temperature of an FG plate with an elliptic cutout is lower than pure ceramic plate and higher than pure metal plate. By rising the percentage of ceramic constituent, the material thermal strength increases.

## REFERENCES

- [1] Bodaghi M., Saidi A.R., 2010, Levy-type solution for buckling analysis of thick functionally graded rectangular plates based on the higher-order shear deformation plate theory, *Applied Mathematical Modelling* **34**: 3659-3673.
- [2] Samsam Shariat B.A., Eslami M.R., 2006, Thermal buckling of imperfect functionally graded plates, *International Journal of Solids and Structures* **43**: 4082-4096.
- [3] Weibgraebra P., Mittelstedt C., Beckera W., 2012, Buckling of composite panels: A criterion for optimum stiffener design, *Aerospace Science and Technology* **16**(1):10-18.
- [4] Zhao X., Lee Y.Y., Liew K.M., 2009, Mechanical and thermal buckling analysis of functionally graded plates, *Composite Structures* **90**: 161-171.
- [5] Ghosh M.K., Kanoria M., 2009, Analysis of thermoelastic response in a functionally graded spherically isotropic hollow sphere based on Green–Lindsay theory, *Acta Mechanica* **207**: 51-67.
- [6] Mahdavian M., 2009, Buckling analysis of simply-supported functionally graded rectangular plates under non-uniform in-plane compressive loading, *Journal of Solid Mechanics* **1**(3):213-225.
- [7] Samsam Shariat B.A., Eslami M.R., 2007, Buckling of thick functionally graded plates under mechanical and thermal loads, *Composite Structures* **78**: 433-439.
- [8] Xiang S., Kang G., 2013, A nth-order shear deformation theory for the bending analysis on the functionally graded plates, *European Journal of Mechanics A/Solids* **37**:336-343.
- [9] Mozafaria H., Ayob A., 2012, Effect of thickness variation on the mechanical buckling load in plates made of functionally graded materials, *Procedia Technology* **1**: 496-504.
- [10] Raki M., Alipour R., Kamanbedast A., 2012, Thermal buckling of thin rectangular FGM plate, *World Applied Sciences Journal* **16**(1): 52-62.
- [11] Avci A., Sahin O.S., Uyaner M., 2005, Thermal buckling of hybrid laminated composite plates with a hole, *Composite Structures* **68**: 247-254.

- [12] Zhen W., Wanji C., 2009, Stress analysis of laminated composite plates with a circular hole according to a single-layer higher-order model, *Composite Structures* **90**: 122-129.
- [13] Kiani Y., Eslami M.R., 2013, An exact solution for thermal buckling of annular FGM plates on an elastic medium, *Composites: Part B* **45**:101-110.
- [14] Thai H.T., Choi D.H., 2012, An efficient and simple refined theory for buckling analysis of functionally graded plates, *Applied Mathematical Modelling* **36**: 1008-1022.
- [15] Saji D., Varughese B., 2008, Finite element analysis for thermal buckling behaviour in functionally graded plates with cut-outs, *Proceedings of the International Conference on Aerospace Science and Technology*, Bangalore India.
- [16] Natarajan S., Chakraborty S., Ganapathi M., Subramanian M., 2014, A parametric study on the buckling of functionally graded material plates with internal discontinuities using the partition of unity method, *European Journal of Mechanics - A/Solids* **44**: 136-147.
- [17] Zenkour A. M., Mashat D. S., 2010, Thermal buckling analysis of ceramic-metal functionally graded plates, *Natural Science* **2**(9):968-978.
- [18] Saidi A. R., Baferani A. H., 2010, Thermal buckling analysis of moderately thick functionally graded annular sector plates, *Composite Structures* **92**:1744-1752.
- [19] Park J.S., Kim J.H., 2006, Thermal post buckling and vibration analyses of functionally graded plates, *Journal of Sound and Vibration* **289**: 77-93.
- [20] Yang J., Shen H.S., 2002, Vibration characteristics and transient response of shear-deformable functionally graded plates in thermal environments, *Journal of Sound and Vibration* **255**:579-602.
- [21] Reddy J. N., 2006, *Theory and Analysis of Elastic Plates and Shells*, Second edition, CRC press.
- [22] Efraim E., Eisenberger M., 2007, Exact vibration analysis of variable thickness thick annular isotropic and FGM plates, *Journal of Sound and Vibration* **299**:720-738.
- [23] Logan D. L., 2010, *A First Course in the Finite Element Method*, Fourth edition.